A porphyrin-PEG polymer with rapid renal clearance

CrossMark

Haoyuan Huang [a, b], Reinier Hernandez [c], Jumin Geng [a], Haotian Sun [b], Wentao Song [a], Feng Chen [c], Stephen A. Graves [c], Robert J. Nickles [c], Chong Cheng [b], Weibo Cai [c], Jonathan F. Lovell [a, b, *]

[a] Department of Biomedical Engineering, University at Buffalo, State University of New York, Buffalo, NY, USA
[b] Department of Chemical and Biological Engineering, University at Buffalo, State University of New York, Buffalo, NY, USA
[c] Department of Radiology and Medical Physics, University of Wisconsin, Madison, WI, USA

ARTICLE INFO

ABSTRACT

Tetracarboxylic porphyrins and polyethylene glycol (PEG) diamines were crosslinked in conditions that gave rise to a water-soluble porphyrin polyamide. Using PEG linkers 2 kDa or larger prevented fluorescence self-quenching. This networked porphyrin mesh was retained during dialysis with membranes with a 100 kDa pore size, yet passed through the membrane when centrifugal filtration was applied. Following intravenous administration, the porphyrin mesh, but not the free porphyrin, was rapidly cleared via renal excretion. The process could be monitored by fluorescence analysis of collected urine, with minimal background due to the large Stokes shift of the porphyrin (230 nm separating excitation and emission peaks). In a rhabdomyolysis mouse model of renal failure, porphyrin mesh urinary clearance was significantly impaired. This led to slower accumulation in the bladder, which could be visualized non-invasively via fluorescence imaging. Without further modification, the porphyrin mesh was chelated with ^{64}Cu for dynamic whole body positron emission tomography imaging of renal clearance. Together, these data show that small porphyrin-PEG polymers can serve as effective multimodal markers of renal function.

© 2015 Elsevier Ltd. All rights reserved.

1. Introduction

The prevalence of advanced renal disease is common and generally affects between 1 and 2 people per thousand, worldwide [1]. The kidneys perform several vital tasks including removal of circulating waste products from blood. This is achieved through glomerular filtration, which is also considered the best general measure of kidney function [2]. While elevated serum levels of endogenous biomolecules such as creatine, urea and cystatin C (normally excreted by the kidney) suggest renal impairment, excretion of an intravenously administered exogenous chemical is preferred to accurately measure the glomerular filtration rate (GFR). Exogenous clinical markers for GFR determination include inulin, dextrans, chelated metals, and iodine molecules, sometimes which are radiolabeled for facilitated detection [3]. The clinical utility of such methods, which are considered gold-standard, has

been called into question due in part to difficulty in administering those tests, which require arduous blood sampling [4].

For over 50 years, the effect of dextran size on renal clearance has been studied in humans [5]. Renal excretion of dextrans over 50 kDa is negligible, whereas excretion of dextrans smaller than 15 kDa is rapid [6,7]. It was shown in rats that neutral dextrans with diameters less 5 nm are cleared renally, whereas those greater than 8 nm are retained in blood circulation [8]. Recently, functional nanoparticles have been explored in this context, since these hold promise for theranostic applications [9]. Luminescent quantum dots with hydrodynamic diameters of less than 5.5 nm have been shown to be efficiently cleared renally [10]. Renal clearance has been demonstrated for numerous other types of appropriately-sized nanoscale materials, including, for example, gold nanoparticles [11], carbonaceous dots [12], biodegradable silicon nanoparticles [13], gold nanoclusters [14], inorganic nanodots [15] and nanotubes [16]. Iron oxide nanoparticles have been explored as diagnostic agents for obstructive nephropathy [17]. Perfluorocarbon nanoparticles were demonstrated to assess intrarenal nonperfusion and vascular leakage in acute kidney injury [18].

Porphyrins and tetrapyrrolic derivatives have long been used as

theranostic agents [19,20]. Polymeric porphyrin structures have been created by cross-linking tetra-functional porphyrins with bi-functional linkers [21–23]. These can provide for high density porphyrin materials for applications such as fluorescence imaging [24,25] and oxygen concentration monitoring [26,27]. Meso-tetra(4-carboxyphenyl) porphyrin (mTCPP) is a water soluble porphyrin derivative that can self-assemble in aqueous systems induced by pH changes [28] and can coordinate with metal ions [29–31]. Attachment to polyethylene glycol (PEG) has been shown to improve monomer stability [32]. We previously demonstrated that PEG diamines can crosslink mTCPP to form a fully insoluble, biocompatible hydrogel polymer for in vivo biosensing applications [24,27]. In this work, we report the development and character-ization of a soluble mTCPP-PEG polymeric mesh for use as a multimodal marker for renal function.

2. Materials and methods

2.1. Materials

Unless specified, reagents were obtained from Sigma. Meso-tetra(4-carboxyphenyl) porphyrin (mTCPP) was obtained from Frontier Scientific, Inc. (Logan, UT, U.S.A.). Polyethylene glycol (PEG)-10000, 6000, 3000, 2000, 1000, 800, 600 and 400 were ob-tained from Rapp Polymere (Tuebingen, Germany). (PEO)$_4$-bis-amine (PEG-192) and (PEO)$_3$-Bis-amine (PEG-148) was obtained from Chem-Impex International (Wood Dale, IL, U.S.A.). O-(Benzo-triazol-1-yl)-N,N,N′,N′-tetramethyluronium hexafluorophosphate (HBTU) was obtained from Advanced Chem Tech Inc (Louisville, KY, U.S.A.). Glycerol was obtained from Bioshop Canada Inc. (Burling-ton, ON, Canada). ICR mice were ordered from Harlan Laboratories Inc. (U.S.A.).

2.2. Synthesis of the mTCPP-PEG polyamide

mTCPP, PEG-diamine and HBTU were dissolved separately in dimethylformamide to make 3 mM, 6 mM and 12 mM stock solu-tions, respectively. 300 μL each of mTCPP and HBTU stock solutions were mixed together with sonication. 4.5 μL N,N-Diisopropylethylamine (DIPEA) was then added into the mixture. 5 min later, 300 μL of the PEG-diamine solution was added drop-wise into the mixture over the course of approximately 2 min. The reaction was carried out with sonication in a water bath at 25 °C for 45 min. The products were put into dialysis tubing with a molecular weight cutoff (MWCO) size of 12 kDa (purchased from Fisherbrand, Fisher Scientific) and dialyzed extensively in deionized water to remove the unincorporated reactants and exchange dime-thylformamide to an aqueous system. The dialyzed products were then centrifuged at 10,000 rpm for 10 min. The supernatant was removed and each milliliter of solution was combined with 200 μL of 10 mM sodium citrate (pH = 4) in order to induce precipitation of any unreacted mTCPP. Following 15 min of shaking, the solutions were centrifuged again at 10,000 rpm for 15 min and the super-natant was collected and re-dialyzed in deionized water to remove sodium citrate.

2.3. Porphyrin-mesh characterization

Porphyrin-PEG mesh (PEG lengths of 10K, 6K, 3K, 2K, 1K, 800, 600, 400, 192 or 148 Da) and mTCPP alone were dissolved in 10 mM Tris–HCl, pH = 8 buffer. The absorbance of the samples was adjusted to be near 0.05 based on the Soret band at 420 nm of mTCPP. The fluorescence of all the samples were tested and relative brightness was calculated by dividing the fluorescence intensity by the corresponding absorbance. The relative brightness of

porphyrin-PEG mesh was further normalized to the relative brightness of free mTCPP alone.

For dialysis and retention experiments, porphyrin-PEG2K mesh was dialyzed with dialysis membranes with a MWCO of 10 kDa (purchased from Fisherbrand, Fisher Scientific UK Ltd) or MWCO of 100 kDa (purchased from Spectra/Por Biotech, U.S.A). Alternatively, the samples were subjected to centrifugal filtration with mem-branes with a MWCO of 10 kDa or 100 kDa (MCP010C41 (10 kDa) and MCP100C41 (100 kDa), Pall Corporation, U.S.A.), respectively. Dialysis groups were dialyzed in water with water changes every 4 h for 12 h. Centrifugation groups were centrifuged at 2500× g for 15 min 3 times. Absorbance of the retentates was then assessed and compared to the initial absorbance. All samples before and after dialysis and centrifugation were adjusted to the same volume.

Sizing of the porphyrin-PEG2K mesh was achieved by gel permeation chromatography (GPC). Data were obtained from a Viscotek GPC system equipped with a VE-3580 refractive index detector, a VE 1122 pump, and two mixed-bed organic columns (PAS-103M and PAS-105M). Dimethylformamide containing 0.1 M LiBr was used as the mobile phase with a flow rate of 0.5 mL/min at 57 °C. The GPC instrument was calibrated using narrowly-dispersed linear polystyrene standards purchased from Varian. Nuclear magnetic resonance (NMR) data was acquired with a Varian Inova-500 spectrometer, using D6-dimethyl sulfoxide as the solvent. Scanning electron micrographs were acquired with a Zeiss AURIGA focused ion beam scanning electron microscope following sample freeze drying from water.

2.4. Characterization of renal clearance

Animal protocols were carried out with the approval of the University at Buffalo IACUC. Porphyrin-PEG2K polyamides were used for all in vivo studies. ICR mice were injected via tail vein with 10 mg/kg porphyrin-PEG2K mesh or mTCPP Tris–HCl solution (pH = 8.0). Mice were then placed in metabolic cages for 24 h with free access to food and water. Urine was collected at 1, 2, 4, 6, 8, 12 and 24 h post-injection. Mice were sacrificed after 24 h and heart, liver, spleen, lung, kidney and feces were extracted for bio-distribution analysis. The organs were also used for hematoxylin and eosin (H&E) stained histology and for cryostat histology.

The acute renal failure model was carried out according to the literature [33]. ICR mice were deprived of water but had free access to food for 16 h 8 mL/kg of a 50% (v/v) glycerol-water solution was distributed equally into the hind limbs via intramuscular injection. The mice were then given free access to water and food for 24 h 10 mg/kg porphyrin-mesh was then injected into ARF mice and urine was collected from metabolic cages. Urine was collected at 1, 2, 4, 6, 8, 12 and 24 h post injection. Heart, liver, spleen, lung, kidney were collected for H&E stained histology and cryostat histology. Whole body fluorescence scanning was performed on mice using an IVIS imaging system with excitation at 430 nm and using the emission signal with the Cy5.5 filter.

2.5. Dynamic PET imaging with ^{64}Cu-porphyrin-mesh

^{64}Cu (t$_{1/2}$ = 12.7 h) was produced in a CTI RDS 112 cyclotron through proton irradiation of ^{64}Ni enriched targets with a specific activity of >5 Ci/μmol. Radiolabeling of porphyrin mesh was accomplished by reacting 4 mCi of ^{64}CuCl$_2$ with 1.5 mg of nano-particle in a NaAc buffer (0.1 M, pH = 5.5) at 37 °C for 2 h, under constant shaking. ^{64}Cu-porphyrin mesh was purified with size exclusion PD-10 columns (GE Healthcare, U.S.A.) using phosphate buffered saline (PBS) as mobile phase. Radioactive fractions were collected for in vivo studies.

In vivo positron emission tomography (PET) imaging studies

were performed in an Inveon microPET/microCT scanner (Siemens Preclinical Solutions, Knoxville, TN, U.S.A.). For dynamic PET studies, normal ICR mice (n = 4) were anesthetized under isoflurane (2%) and their tail vein catheterized. Following, animals were placed in the scanner in a prone position and simultaneously with the injection of 200−300 μCi of ^{64}Cu-porphyrin mesh, a 30 min emission scan was acquired. List mode files were framed into 28 frames: 5 × 6 s, 7 × 30 s, 6 × 60 s, 6 × 120 s, and 2 × 240 s. Two additional static PET scans at 2 and 4 h post-injection of the tracer were acquired. Dynamic and static scans were reconstructed using an ordered subset expectation maximization 3D/maximum a posteriori (OSEM3D/MAP) reconstruction algorithm. Region-of-interest (ROI) analysis of the PET images was performed to determine time activity curves for blood pool, liver, kidney, and muscle. Tissue uptakes were expressed as percentage of the injected dose per gram (% ID/g). An imaging-based approach which estimates the arterial concentration of the radiotracer from ROIs of the heart, was employed to determine the blood pharmacokinetics (PK) of the radiolabelled mesh. Circulation half-life was derived from the slow rate constant of the bi-exponential fitting of heart time−activity curve.

For *ex vivo* biodistribution studies, another cohort of 3 mice was injected with 50 μCi of ^{64}Cu-porphyrin mesh and placed in metabolic cages. Mice were sacrificed 4 h post-injection and all major tissues along with urine and feces collected and the radioactivity counted in an automated γ-counter (Perkin Elmer). Tissue distribution was reported as percentage of the injected dose (% ID).

3. Results and discussion

### 3.1. Synthesis and characterization of the porphyrin mesh

The synthetic reaction of the porphyrin-PEG polyamide is shown as Fig. 1A. The ratio of mTCPP:PEG:HBTU was 1:2:4, which corresponds to equimolar ratios of functional groups of the tetracarboxylic porphyrin, the PEG diamine and the HBTU acid activator. Unlike conventional approaches which graft porphyrins onto existing polymers [34], mTCPP serves as the polymer comonomer. The resulting product is a random polyamide network of PEG and porphyrin, which is reminiscent of a mesh material. As shown in Fig. 1B, at polymerization concentrations equal to or greater than 2 mM porphyrin, essentially all the mTCPP became incorporated into a single insoluble crosslinked polymer, consistent with previous studies [24,27]. However, when polymerization was carried out using just 1 mM mTCPP, the resulting polymer was 100% soluble without any detectable aggregation. The products were then dialyzed with a membrane with 12 kDa pore size. The dialysis step exchanged the polymer from dimethylformamide into water, and also enabled the removal of non-polymerized small molecules and reactants. This procedure was carried out with different sized PEG diamines of 6, 2 and 0.6 kDa size. As shown in Fig. 1C, despite differences in linker sizes, all the PEG diamines produced highly soluble polymers with good yield. When HBTU was omitted from the reaction, no polymerization occurred and the porphyrin mesh yield was negligible. Likewise, in the absence of PEG diamine, no polymer was produced.

This procedure was then carried out with 10 different PEG diamines, ranging in size from 150 Da to 10 kDa. The brightness of the resulting porphyrin mesh was then determined (Fig. 1D). A clear decrease in the brightness was observed in those formed from PEG-diamines smaller than 2 kDa. This is likely due to self-quenching induced by intermolecular porphyrin interactions crosslinked with short PEG linkers. Thus, the porphyrin mesh generated with the 2 kDa PEG diamine was used for further studies.
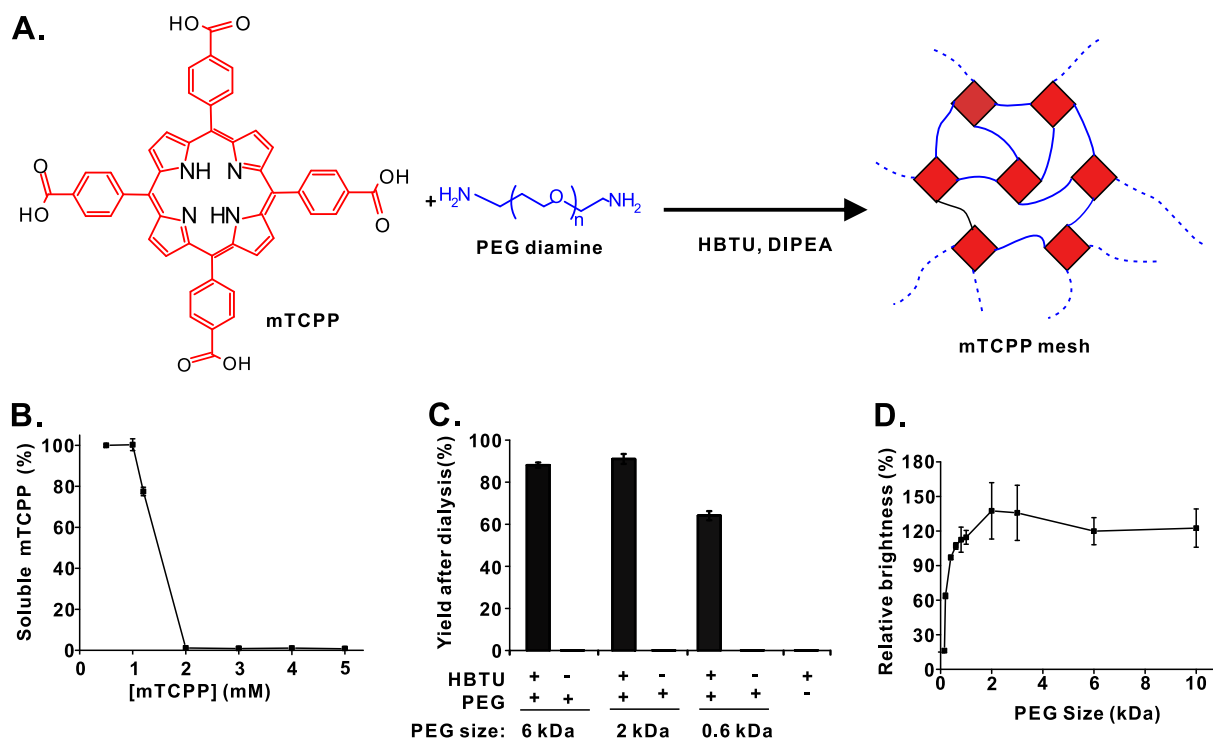
Fig. 1. Development of a high density, soluble porphyrin-PEG polyamide mesh. A) Schematic of the porphyrin-PEG mesh reaction. The ratio of mTCPP (red) to PEG-diamine (blue) to HBTU was 1:2:4. B) Soluble polymer generation as a function of mTCPP concentration during polymerization reaction of mTCPP and PEG6K diamine. All reactants were kept at the same ratio. C) Product yields following dialysis for PEG-diamines of indicated lengths; D) Relative brightness of mTCPP-PEG polyamides formed with dialyzed PEG-diamines of the indicated molecular weights (10K, 6K, 3K, 2K, 1K, 800, 600, 400, 192 and 148 Da) relative to free mTCPP. Data show mean +/− std. dev. for n = 3 separate polymerization reactions and purifications. (For interpretation of the references to color in this figure legend, the reader is referred to the web version of this article.)
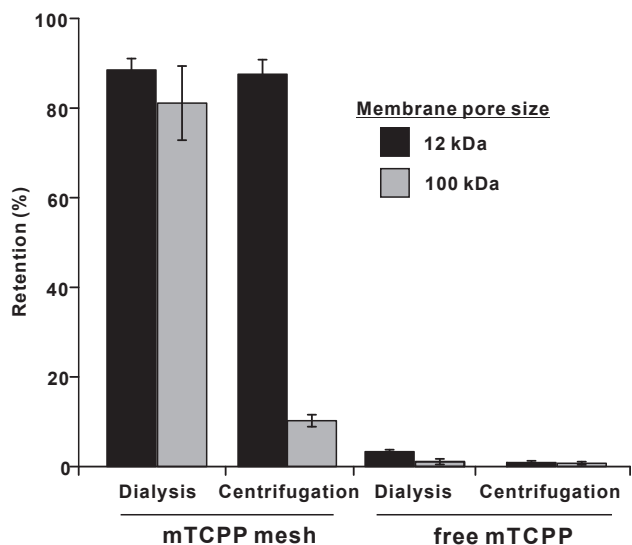
Fig. 2. Porphyrin mesh and monomer retention during dialysis and centrifugal filtration. Samples were subjected to dialysis or centrifugal filtration with the indicated membranes and retention was calculated based on absorption values. Mean +/− std. dev. for n = 3 (for porphyrin mesh, these represent 3 separate preparations).

Based on gel permeation chromatography in dimethylformamide, the porphyrin mesh (generated with the 2 kDa PEG linker) had a relatively broad size distribution with a number-average molecular weight of 16.2 kDa (Fig. S1). The proton NMR signals from the mTCPP carboxylic acid groups (close to 12 ppm) were absent in the mesh product, showing that these functional groups reacted (Fig. S2). Expected and observed CHN elemental analysis data are shown in Table S1. Scanning electron microscopy of the freeze dried mesh demonstrates a polydisperse spherical microstructure of the mesh agglomerates (Fig. S3). Compared to the free mTCPP (which is fully water soluble at pH 8), the porphyrin-PEG-2K mesh displayed a similar absorption spectrum (Fig. S4). Together with the lack of fluorescence self-quenching (Fig 1D), the data suggest the porphyrins within the mesh did not interact sufficiently to induce modified spectral properties, possibly due to the spatial arrangement and confinement of the porphyrin and PEG in a three dimensional mesh.

The susceptibility of the porphyrin mesh to pass through porous membranes was examined with dialysis and centrifugal filtration. As shown in Fig. 2, with membranes with relatively small pores of approximately 10 kDa, retention of the porphyrin mesh was ~90% for both conventional dialysis and centrifugal centrifugation. When membranes with larger 100 kDa pores were used, the sample was retained in dialysis but could pass through the membrane when

centrifugal filtration was applied. Free mTCPP could pass through all membranes with either dialysis or centrifugal filtration. These data suggest that the polymer size of the porphyrin-mesh was greater than 10 kDa, in accordance with GPC results, which indicated an average size of 16.2 kDa. The reason the mesh could be retained in 100 kDa membranes during dialysis can be attributed to higher order polymer self-assembly characteristics which was disrupted by the force of centrifugal filtration.

### 3.2. Renal clearance of the porphyrin mesh

Unlike commonly used markers for renal function, the porphyrin mesh exhibits strong endogenous fluorescence. Excitation and emission spectra are shown in Fig. 3A. The Stokes shift separating excitation and emission was 230 nm, with peak excitation and emission wavelengths of 420 nm and 650 nm, respectively. This large shift makes fluorescence measurements of urine straightforward without interference and is conducive for in vivo imaging. A white light and fluorescence photograph of the porphyrin mesh solution is presented in Fig. 3B. Mice were intravenously injected with 10 mg/kg porphyrin mesh, and placed in a metabolic cage with free access to food and water and urine was collected periodically over 24 h. As shown in Fig. 3C, close to 70% of the porphyrin mesh injected dose was recovered in excreted urine within 2 h of administration. Little additional polymer was excreted between the initial 2 h and the 24 h time point. The fraction of porphyrin mesh that was not cleared could possibly represent larger polymerized porphyrins that were too large for renal clearance. In the future, additional purification steps could potentially be added to enhance renal clearance. When free mTCPP was administered, little was recovered in the urine. This is likely because the small molecule is able to bind to serum components to prevent rapid excretion. The biodistribution of the porphyrin mesh was assessed following organ homogenization, and nearly all the recovered porphyrin signal was confined to the urine, with negligible amounts detected in the heart, liver, spleen, lung, kidney or feces (Fig. 3D). Urine that contained the excreted porphyrin mesh was dialyzed and exhibited similar retention pattern as the freshly prepared polymer (Fig. 2) which demonstrates the intactness of the porphyrin-PEG2K mesh in urine (Fig. 3E). Just as the porphyrin mesh could pass through the membrane upon centrifugal filtration, the porphyrin mesh apparently could dynamically disassemble while circulating in vivo to pass through the glomerular membrane.

Acute renal failure (ARF) is often accompanied with a rapid defect in glomerular filtration [35,36]. Although ARF can be reversible, it can lead to chronic kidney damage and can damage other organs [37,38]. ARF is typically diagnosed by testing for high
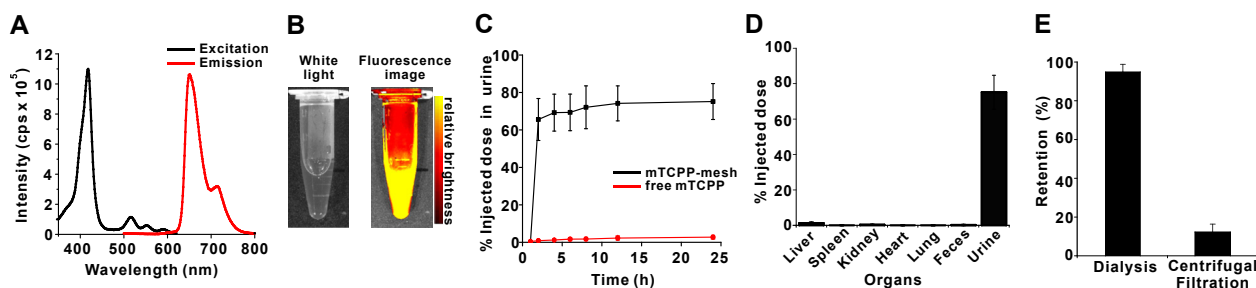
Fig. 3. Fluorescence Monitoring of Porphyrin mesh renal clearance. A) Fluorescence excitation and emission spectra of the PEG-2K porphyrin mesh in water. B) White light and fluorescence photographs of the PEG-2K porphyrin mesh solution. C) Urinary excretion of porphyrin mesh or free mTCPP following intravenous injection of 10 mg/kg doses (mean+/− std. dev. for n = 3 mice); D) Biodistribution from tissue homogenates 24 h after porphyrin-mesh injection (mean+/− std. dev. for n = 3 mice). E) Retention of porphyrin-PEG2K mesh in recovered urine after dialysis or centrifugal filtration using membranes with 100 kDa pore size. Values show mean +/− std. dev. for n = 3.
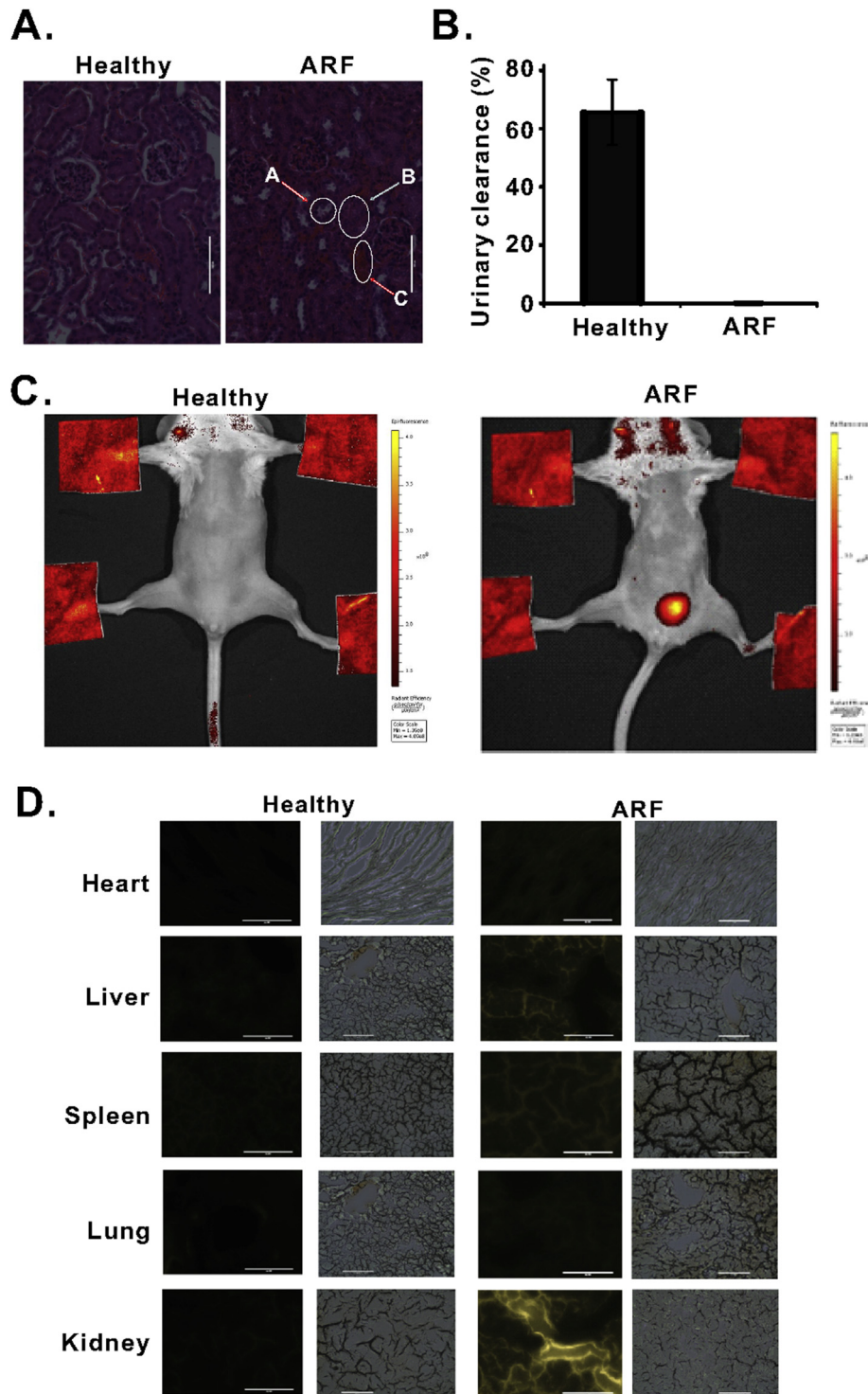
Fig. 4. Inhibited porphyrin mesh excretion in an acute renal failure (ARF) model. A) H&E stained kidney histology of normal and ARF mice, "A" shows partially renal tubular epithelium degeneration and cast deformation, "B" shows tubular necrosis and "C" demonstrates angiectasis and inflammation. 100 μm scale bar is shown. B) Fluorescence analysis of urine in mice 2 h after intravenous injection of porphyrin mesh (10 mg/kg) (mean +/− std. dev. for n = 3); C) Whole body fluorescence scan 24 h after injection of porphyrin-PEG mesh in mice. Representative images for n = 3 mice. D) Fluorescence and white light images of frozen sections of indicated organs. 100 μm scale bar is shown.

levels of circulating urea or creatinine, or monitoring decreasing urine output [39,40]. However, these tests might only yield positive results with sufficient time lapse from ARF onset so there is interest in finding better ARF markers [41–44].

A glycerol-induced myohemoglobinuria model of ARF was used that leads to acute tubular necrosis [45,46]. Even though the exact mechanism is unclear, glycerol-induced ARF is thought to be caused by myohemoglobinuria-induced glomerular filtration failure [47]. The morphology of glomerular of normal and ARF mice is shown in Fig. 4A. Under 40X magnification, compared to the H&E stained histology of normal mouse kidneys, the morphology of kidneys of ARF mice showed tubular necrosis, cast deformations and
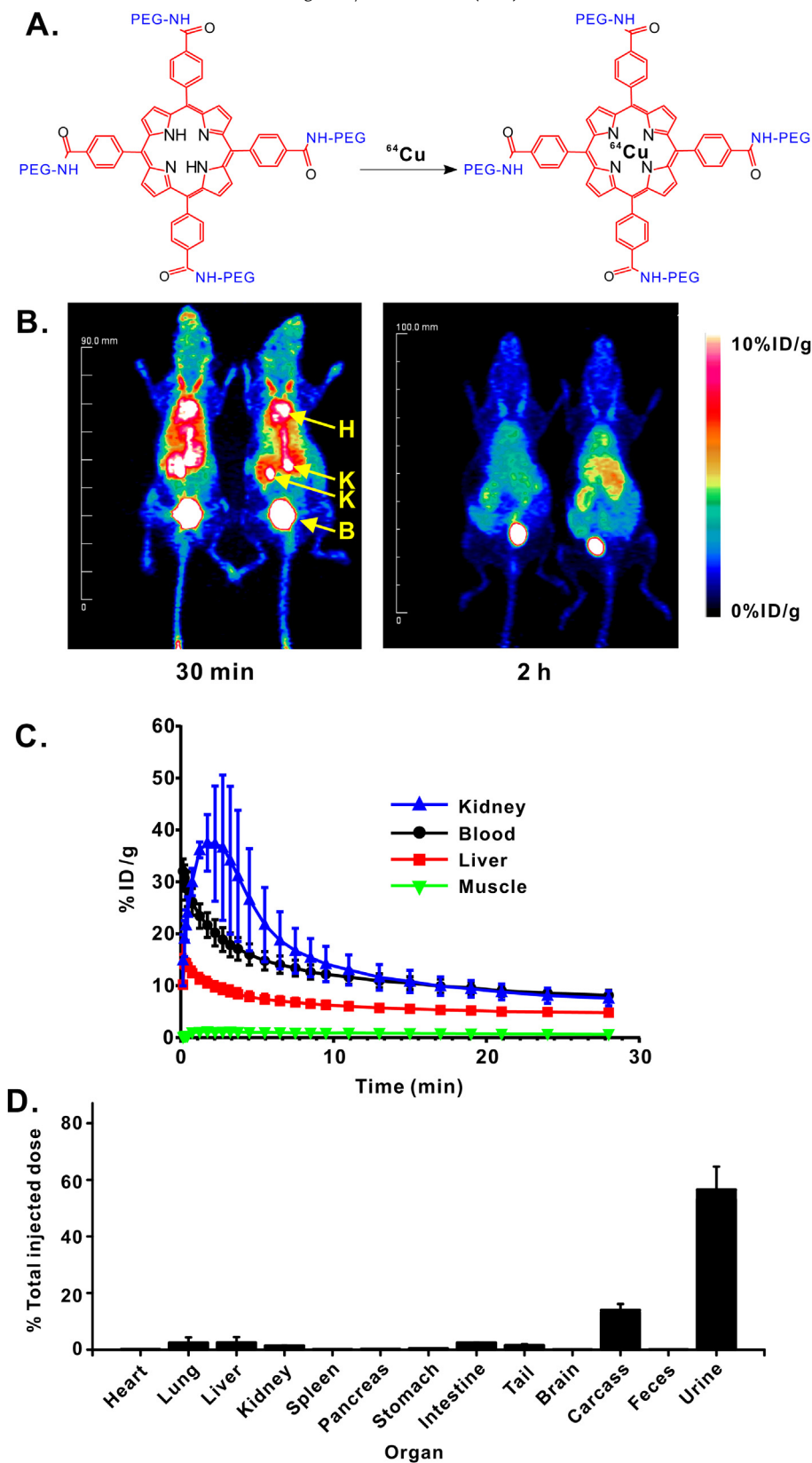
Fig. 5. ^{64}**Cu-labeled porphyrin mesh**. A) Facile post chelation strategy for inserting ^{64}Cu into the porphyrin mesh; B) Representative PET images of mice 30 min and 2 h post intravenous injection of ^{64}Cu-porphyrin-PEG mesh. Heart (H), Kidneys (K) and bladder (B) are indicated. C) Dynamic PET imaging reveals ^{64}Cu distribution in indicated organs (mean +/− std. dev. for n = 4 mice); D) ^{64}Cu biodistribution of extracted organs 4 h after intravenous injection of ^{64}Cu-porphyrin mesh (mean +/− std. dev. for n = 3 mice).

inflammation. Following intravenous administration of the porphyrin mesh, the fluorescence in the urine of the two groups of mice was dramatically different after 2 h (Fig. 4B). The porphyrin mesh output in urine in healthy mice was over 60 times that of ARF mice. 24 h after porphyrin mesh administration, normal mice and ARF mice were subjected to whole body, non-invasive fluorescence

imaging (Fig. 4C). The bladder of all ARF mice examined were fluorescent due to impaired and slower renal excretion of the porphyrin mesh. The mesh could be readily detected in the bladder with non-invasive fluorescence imaging. The mesh could not be visualized in the kidneys of the ARF mice, probably due to their deeper localization in the body. Even though the mesh has red fluorescence emission, the blue excitation maximum is not optimal for in vivo imaging and future work could benefit from development of probes that operate in the near infrared with both excitation and emission [48]. As expected, no signal was visualized in the bladder healthy mice, since they had already cleared the porphyrin mesh after a just a couple of hours. 24 h following porphyrin mesh administration, hearts, livers, spleens, lungs and kidneys of both healthy and ARF mice were examined with frozen sectioning and white light and florescence analysis. As shown in Fig. 4D, fluorescent signals from healthy mice organs were too weak to be detected. However, strong porphyrin fluorescence was detected in the kidneys of the ARF mice, but not any other organs. Thus, the porphyrin mesh distinguished ARF mice from healthy mice on the basis of analytical examination of urine, non-invasive in vivo imaging, and fluorescent histology analysis.

3.3. In vivo PET imaging with ^{64}Cu-labeled porphyrin mesh

Porphyrins and related tetrapyrrolic nanoparticles can chelate copper for convenient post-labeling with ^{64}Cu, a useful PET radionuclide with a 12.7 h half-life [49–51]. As shown in Fig. 5A, the mesh was labeled with simple aqueous incubation with ^{64}Cu. Fig. 5B shows representative maximum intensity projection (MIP) of coronal PET images depicting the in vivo biodistribution of ^{64}Cu-porphyrin mesh, 30 min and 2 h after intravenous administration (n = 4). ROI analysis of the static images unveiled a prominent accumulation of the mesh within blood pool (8.2 ± 1.0 %ID/g), kidneys (7.5 ± 1.4 %ID/g), and bladder at early time points, which gradually decayed overtime to 2.9 ± 0.2 %ID/g and 3.2 ± 0.2 %ID/g for blood and kidney respectively, 4.5 h post-injection (Fig. S5). Other background tissues such as liver and muscle presented a lower, steadier uptake of the radiolabeled mesh indicating the non-specific character of such accretion. Quantitative analysis of the dynamic PET data enables us to unequivocally establish renal clearance as the primary excretion route of the porphyrin mesh from the mouse body, and determine pharmacokinetic parameters including blood circulation half-life. The video in the Supplementary Information shows the time progression of the ^{64}Cu-porphyrin mesh biodistribution within 4 h after administration into mice. An initially high concentration of the mesh in the blood pool was observed (32.1 ± 2 %ID/g) that rapidly filtered through the kidneys and accrued in the bladder. The rate of clearance of the ^{64}Cu-porphyrin mesh from the blood compartment was determined by fitting the dynamic time–activity curves of the heart to a two-phase exponential decay (Fig. 5C, Fig. S6) and a blood circulation half-life of just 7.4 min was observed.

A supplementary video related to this article can be found at http://dx.doi.org/10.1016/j.biomaterials.2015.10.049.

Ex vivo biodistribution studies were performed to corroborate the accuracy of PET imaging data and to provide a detailed distribution of the labeled mesh within all major organs. Mice (n = 3) were sacrificed 4 h after inoculation of the tracer and the radioactivity corresponding to urine, feces, and all major organs recorded (Fig. 5D). The ^{64}Cu-porphyrin mesh radioactivity collected in urine (~60 %ID) was markedly higher compared to the rest of the collected samples, which showed marginal accumulations (<5 %ID). Altogether, data were comparable with respect to *ex vivo* biodistribution, fluorescence imaging (Fig. 3D), and the PET imaging, which showed the maximum accumulation of the porphyrin mesh

in urine, and low uptake in other organs such as the liver, kidney, heart, blood, and muscles. The consistency of ^{64}Cu-porphyrin mesh renal clearance with fluorometric analysis of unlabeled mesh clearance indicates that the radionuclide chelation is stable and does not alter effective renal clearance.

4. Conclusion

In this work we presented a facile synthetic route to a high-density water soluble porphyrin polyamide mesh. By using appropriate sized PEG linkers (e.g. 2 kDa) porphyrin fluorescence self-quenching was avoided. Upon centrifugal filtration but not dialysis, the porphyrin mesh (and the porphyrin mesh recovered from urine) could pass through membranes with pore sizes of 100 kDa. Upon intravenous administration to mice, the mesh, but not the free porphyrin, was excreted in urine. Renal clearance was rapid and effective, with more than 60% of the injected dose cleared in urine within a couple of hours. Administered porphyrin mesh could be used to distinguish healthy mice from those with acute renal failure by fluorescence analysis of urine, in vivo optical imaging and fluorescence analysis of kidney sections. The porphyrin mesh was seamlessly labeled with ^{64}Cu for whole body PET imaging and biodistribution, confirming that little mesh remained in vital organs following clearance. Future work includes achieving more monodisperse polymer sizes in order to further improve the renal clearance of the mesh and chelation of other metals into the mesh such as manganese to enable magnetic resonance contrast for higher order multimodal imaging approaches [52]. Overall, porphyrin mesh holds potential as a unique biomaterial for monitoring and imaging renal function.

Appendix A. Supplementary data

Supplementary data related to this article can be found at http://dx.doi.org/10.1016/j.biomaterials.2015.10.049.

References

[1] A.S. Levey, J. Coresh, Chronic kidney disease, Lancet 379 (2012) 165–180.
[2] S.I. Hallan, R.T. Gansevoort, Moderator's view: estimating glomerular filtration rate—the past, present and future, Nephrol. Dial. Transplant. 28 (2013) 1404–1406.
[3] C.P. Price, H. Finney, Developments in the assessment of glomerular filtration rate, Clin. Chim. Acta 297 (2000) 55–66.
[4] C-y Hsu, N. Bansal, Measured GFR as "Gold Standard"—all that glitters is not gold? Clin. J. Am. Soc. Nephrol. 6 (2011) 1813–1814.
[5] G. Arturson, G. Wallenius, The renal clearance of dextran of different molecular sizes in normal humans, Scand. J. Clin. Lab. Investig. 16 (1964) 81–86.
[6] J.K. Leypoldt, R.P. Frigon, K.W. Devore, L.W. Henderson, A rapid renal clearance methodology for dextran, Kidney Int. 31 (1987) 855–860.
[7] C.E. Mogensen, The glomerular permeability determined by dextran clearance using sephadex gel filtration, Scand. J. Clin. Lab. Investig. 21 (1968) 77–82.
[8] R.L. Chang, I.F. Ueki, J.L. Troy, W.M. Deen, C.R. Robertson, B.M. Brenner, Permselectivity of the glomerular capillary wall to macromolecules. II. Experimental studies in rats using neutral dextran, Biophys. J. 15 (1975) 887–906.
[9] J. Xie, S. Lee, X. Chen, Nanoparticle-based theranostic agents, Adv. Drug Deliv. Rev. 62 (2010) 1064–1079.
[10] H. Soo Choi, W. Liu, P. Misra, E. Tanaka, J.P. Zimmer, B. Itty Ipe, et al., Renal clearance of quantum dots, Nat. Biotechnol. 25 (2007) 1165–1170.
[11] C. Zhou, M. Long, Y. Qin, X. Sun, J. Zheng, Luminescent gold nanoparticles with efficient renal clearance, Angew. Chem. 123 (2011) 3226–3230.
[12] H. Chen, G.D. Wang, W. Tang, T. Todd, Z. Zhen, C. Tsang, et al., Gd-encapsulated carbonaceous dots with efficient renal clearance for magnetic resonance imaging, Adv. Mater. 26 (2014) 6761–6766.

[13] J.-H. Park, L. Gu, G. von Maltzahn, E. Ruoslahti, S.N. Bhatia, M.J. Sailor, Biodegradable luminescent porous silicon nanoparticles for in vivo applications, Nat. Mater. 8 (2009) 331–336.

[14] X.-D. Zhang, D. Wu, X. Shen, P.-X. Liu, F.-Y. Fan, S.-J. Fan, In vivo renal clearance, biodistribution, toxicity of gold nanoclusters, Biomaterials 33 (2012) 4628–4638.

[15] H. Xing, S. Zhang, W. Bu, X. Zheng, L. Wang, Q. Xiao, et al., Ultrasmall NaGdF4 nanodots for efficient MR angiography and atherosclerotic plaque imaging, Adv. Mater. 26 (2014) 3867–3872.

[16] A. Ruggiero, C.H. Villa, E. Bander, D.A. Rey, M. Bergkvist, C.A. Batt, et al., Paradoxical glomerular filtration of carbon nanotubes, Proc. Natl. Acad. Sci. 107 (2010) 12369–12374.

[17] O. Hauger, C. Delalande, C. Deminière, B. Fouqueray, C. Ohayon, S. Garcia, et al., Nephrotoxic nephritis and obstructive nephropathy: evaluation with mr imaging enhanced with ultrasmall superparamagnetic iron oxide—preliminary findings in a rat model, Radiology 217 (2000) 819–826.

[18] L. Hu, J. Chen, X. Yang, A. Senpan, J.S. Allen, N. Yanaba, et al., Assessing intrarenal nonperfusion and vascular leakage in acute kidney injury with multinuclear 1H/19F MRI and perfluorocarbon nanoparticles, Magn. Reson. Med. 71 (2014) 2186–2196.

[19] Y. Zhang, J.F. Lovell, Porphyrins as theranostic agents from prehistoric to modern times, Theranostics 2 (2012) 905–915.

[20] H. Huang, W. Song, J. Rieffel, J.F. Lovell, Emerging applications of porphryins in photomedicine, Front. Phys. 3 (2015), http://dx.doi.org/10.3389/fphy.2015.00023.

[21] M. Singh, D. Bandyopadhyay, A cross-linked manganese porphyrin as highly efficient heterogeneous catalyst for selective oxidation of cycloalkenes/alkanes, J. Chem. Sci. 126 (2014) 1707–1713.

[22] Z. Zhang, X. Li, Q. Zhao, J. Ke, Y. Shi, P. Ndokoye, et al., Facile synthesis and characterizations of copper–zinc-10,15,20-tetra(4-pyridyl) porphyrin (Cu–ZnTPyP) coordination polymer with hexagonal micro-lump and micro-prism morphologies, J. Colloid Interface Sci. 432 (2014) 229–235.

[23] Y. Diskin-Posner, I. Goldberg, Porphyrin sieves. Designing open networks of tetra(carboxyphenyl)porphyrins by extended coordination through sodium ion auxiliaries, New J. Chem. 25 (2001) 899–904.

[24] J.F. Lovell, A. Roxin, K.K. Ng, Q. Qi, J.D. McMullen, R.S. DaCosta, et al., Porphyrin-cross-linked hydrogel for fluorescence-guided monitoring and surgical resection, Biomacromolecules 12 (2011) 3115–3118.

[25] F. Lv, L. Mao, T. Liu, Thermosensitive porphyrin-incorporated hydrogel with four-arm PEG–PCL copolymer: preparation, characterization and fluorescence imaging in vivo, Mater. Sci. Eng. C 43 (2014) 221–230.

[26] Y. Tian, B.R. Shumway, W. Gao, C. Youngbull, M.R. Holl, R.H. Johnson, et al., Influence of matrices on oxygen sensing of three sensing films with chemically conjugated platinum porphyrin probes and preliminary application for monitoring of oxygen consumption of Escherichia coli (E. coli), Sens. Actuators B Chem. 150 (2010) 579–587.

[27] H. Huang, W. Song, G. Chen, J.M. Reynard, T.Y. Ohulchanskyy, P.N. Prasad, et al., Pd-porphyrin-cross-linked implantable hydrogels with oxygen-responsive phosphorescence, Adv. Healthc. Mater. 3 (2014) 891–896.

[28] S.C. Doan, S. Shanmugham, D.E. Aston, J.L. McHale, Counterion dependent dye aggregates: nanorods and nanorings of tetra(p-carboxyphenyl)porphyrin, J. Am. Chem. Soc. 127 (2005) 5885–5892.

[29] S. Lipstman, S. Muniappan, S. George, I. Goldberg, Framework coordination polymers of tetra(4-carboxyphenyl)porphyrin and lanthanide ions in crystalline solids, Dalton Trans. (2007) 3273–3281.

[30] Y. Diskin-Posner, S. Dahal, I. Goldberg, New effective synthons for supramolecular self-assembly of -carboxyphenylporphyrins, Chem. Commun. (2000) 585–586.

[31] H.-L. Jiang, D. Feng, K. Wang, Z.-Y. Gu, Z. Wei, Y.-P. Chen, et al., An exceptionally stable, porphyrinic Zr metal–organic framework exhibiting pH-dependent fluorescence, J. Am. Chem. Soc. 135 (2013) 13934–13938.

[32] M.A. Castriciano, A. Romeo, N. Angelini, N. Micali, A. Longo, A. Mazzaglia, et al., Structural features of meso-tetrakis(4-carboxyphenyl)porphyrin Interacting with amino-terminated poly(propylene oxide), Macromolecules 39 (2006) 5489–5496.

[33] K.A. Nath, J.J. Haggard, A.J. Croatt, J.P. Grande, K.D. Poss, J. Alam, The indispensability of heme oxygenase-1 in protecting against acute heme protein-induced toxicity in vivo, Am. J. Pathol. 156 (2000) 1527–1535.

[34] U. Chitgupi, Y. Zhang, C.Y. Lo, S. Shao, W. Song, J. Geng, et al., Sulfonated polyethylenimine for photosensitizer conjugation and targeting, Bioconjugate Chem. 26 (2015) 1633–1639.

[35] S.S. Adiyanti, T. Loho, Acute kidney injury (AKI) biomarker, Acta Med. Indones. 44 (2012) 246–255.

[36] R. Bellomo, J.A. Kellum, C. Ronco, Acute kidney injury, Lancet 380 (2012) 756–766.

[37] S.G. Coca, S. Singanamala, C.R. Parikh, Chronic kidney disease after acute kidney injury: a systematic review and meta-analysis, Kidney Int. 81 (2012) 442–448.

[38] D.P. Basile, D. Donohoe, K. Roethe, J.L. Osborn, Renal ischemic injury results in permanent damage to peritubular capillaries and influences long-term function, Am. J. Physiol. Ren. Physiol. 281 (2001) F887–F899.

[39] J.V. Salgado, F.A. Neves, M.G. Bastos, A.K. França, D.J. Brito, E.M. Santos, et al., Monitoring renal function: measured and estimated glomerular filtration rates — a review, Braz J. Med. Biol. Res. 43 (2010) 528–536.

[40] J. Vanmassenhove, R. Vanholder, E. Nagler, W. Van Biesen, Urinary and serum biomarkers for the diagnosis of acute kidney injury: an in-depth review of the literature, Nephrol. Dial. Transpl. 28 (2013) 254–273.

[41] J.L. Koyner, V.S. Vaidya, M.R. Bennett, Q. Ma, E.M. Worcester, S.A. Akhter, et al., Urinary biomarkers in the clinical prognosis and early detection of acute kidney injury, Clin. J. Am. Soc. Nephrol. 5 (2010).

[42] A. Matheson, M.D.P. Willcox, J. Flanagan, B.J. Walsh, Urinary biomarkers involved in type 2 diabetes: a review, Diabetes Metab. Res. Rev. 26 (2010) 150–171.

[43] Z.H. Endre, J.W. Pickering, R.J. Walker, P. Devarajan, C.L. Edelstein, J.V. Bonventre, et al., Improved performance of urinary biomarkers of acute kidney injury in the critically ill by stratification for injury duration and baseline renal function, Kidney Int. 79 (2011) 1119–1130.

[44] J.S. Ozer, F. Dieterle, S. Troth, E. Perentes, A. Cordier, P. Verdes, et al., A panel of urinary biomarkers to monitor reversibility of renal injury and a serum marker with improved potential to assess renal function, Nat. Biotechnol. 28 (2010) 486–494.

[45] D.E. Oken, M.L. Arce, D.R. Wilson, Glycerol-induced hemoglobinuric acute renal failure in the rat. I. Micropuncture study of the development of oliguria, J. Clin. Investig. 45 (1966) 724–735.

[46] M.C. Korrapati, B.E. Shaner, R.G. Schnellmann, Recovery from glycerol-induced acute kidney injury is accelerated by suramin, J. Pharmacol. Exp. Ther. 341 (2012) 126–136.

[47] R.A. Zager, Rhabdomyolysis and myohemoglobinuric acute renal failure, Kidney Int. 49 (1996) 314–326.

[48] J. Liu, Y. Liu, W. Bu, J. Bu, Y. Sun, J. Du, et al., Ultrasensitive nanosensors based on upconversion nanoparticles for selective hypoxia imaging in vivo upon near-infrared excitation, J. Am. Chem. Soc. 136 (2014) 9701–9709.

[49] Y. Zhang, M. Jeon, L.J. Rich, H. Hong, J. Geng, Y. Zhang, et al., Non-invasive multimodal functional imaging of the intestine with frozen micellar naphthalocyanines, Nat. Nano 9 (2014) 631–638.

[50] J. Rieffel, F. Chen, J. Kim, G. Chen, W. Shao, S. Shao, et al., Hexamodal Imaging with porphyrin-phospholipid-coated upconversion nanoparticles, Adv. Mater. 27 (2015) 1785–1790.

[51] T.W. Liu, T.D. MacDonald, J. Shi, B.C. Wilson, G. Zheng, Intrinsically copper-64-labeled organic nanoparticles as radiotracers, Angew. Chem. Int. Ed. 51 (2012) 13128–13131.

[52] J. Rieffel, U. Chitgupi, J.F. Lovell, Recent advances in higher-order, multimodal, biomedical imaging agents, Small 11 (2015) 4445–4461.